J. Fluid Mech. (2024), *vol*. 993, A2, doi:10.1017/jfm.2024.566

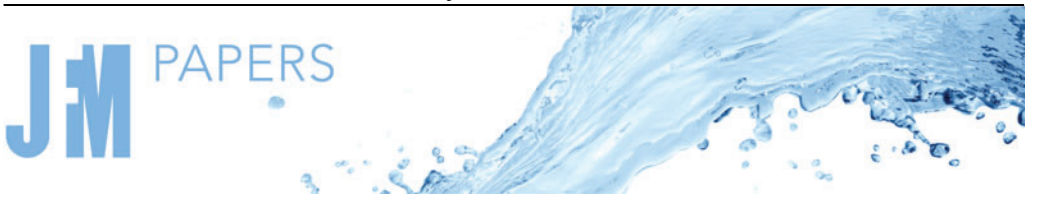

The intrinsic scaling relation between pressure fluctuations and Mach number in compressible turbulent boundary layers

Peng-Jun-Yi Zhang[1], **Zhen-Hua Wan**[1],†, **De-Jun Sun**[1],† **and Xi-Yun Lu**[1]

[1]Department of Modern Mechanics, University of Science and Technology of China, Hefei 230027, PR China

(Received 31 January 2024; revised 14 May 2024; accepted 18 June 2024)

The scaling relations mapping the turbulence statistics in compressible turbulent boundary layers (TBLs) onto their incompressible counterparts are of fundamental significance for turbulence modelling, such as the Morkovin scaling for velocity fields, while for pressure fluctuation fields, a corresponding scaling relation is currently absent. In this work, the underlying scaling relations of pressure fluctuations about Mach number (M) contained in their generation mechanisms are explored by analysing a series of direct numerical simulation data of compressible TBLs over a wide Mach number range ($0.5 \leq M \leq 8.0$). Based on the governing equation of pressure fluctuations, they are decomposed into components according to the properties of source terms. It is notable that the intensity of the compressible component, predominantly originating from the acoustic mode, obeys a monotonic distribution about the Mach number and wall distance; further, the intensity of the rest of the pressure components, which are mainly generated by the vorticity mode, demonstrates a uniform distribution consistent with its incompressible counterpart. Moreover, the coupling between the two components is negligibly weak. Based on the scaling relations, semiempirical models for the fluctuation intensity of both pressure and its components are constructed. Hence, a mapping relation is obtained that the profiles of pressure fluctuation intensities in compressible TBLs can be mapped onto their incompressible counterparts by removing the contribution from the acoustic mode, which can be provided by the model. The intrinsic scaling relation can provide some basic insight for pressure fluctuation modelling.

Key words: compressible boundary layers, turbulent boundary layers

† Email addresses for correspondence: wanzh@ustc.edu.cn, dsun@ustc.edu.cn

1. Introduction

Pressure fluctuations in a compressible turbulent boundary layer (TBL) are a fundamental topic in both turbulence modelling and engineering applications. On the one hand, fluctuating pressure plays an essential role in redistributing the turbulent kinetic energy (Pope 2000) and exchanging between internal and kinetic energy (Zhao, Liu & Lu 2020). On the other hand, pressure fluctuations within subsonic TBLs are the major excitation sources of cabin noise during the cruise stage for aeroplanes, while within supersonic and hypersonic TBLs, they are associated with the cause of acoustic fatigue that structural elements of an aircraft are exposed to (Bull 1996). Accordingly, pressure fluctuations in TBLs have been the subject of extensive investigations in recent decades (Willmarth 1975; Bull 1996; Beresh *et al.* 2011; Bernardini & Pirozzoli 2011; Gloerfelt & Berland 2013; Ritos, Drikakis & Kokkinakis 2019*a*; Gerolymos & Vallet 2023), where one of the most important control parameters is the free stream Mach number M. With M increasing, the acoustic mode and entropy mode can be further excited (Zhang, Duan & Choudhari 2017) and coupled with various flow modes to induce complex flow structures, which are closely related to the generation and evolution of pressure fluctuations. Additionally, increasing M enhances the Mach wave radiation and the Doppler effect to modulate the characteristics of the intensity and sound-radiation directivity. The quantitative assessment of the influence of Mach number on pressure fluctuations is highly advantageous for turbulence modelling and structural design.

The Mach number level can reflect the strength of compressibility effects, which give rise to mean density gradients in addition to mean velocity gradients, and to the turbulent field consisting of pressure, density and velocity fluctuations (Smits 1991). The role of pressure fluctuations in compressible flows becomes more significant due to the additional energy transport mechanisms, such as pressure–dilatation and pressure–strain correlations (Lele 1994). In addition, wall-cooling effects can also strengthen compressibility effects (Yu, Xu & Pirozzoli 2020). Zhang *et al.* (2017) found that the intensity of near-wall pressure fluctuations is dramatically enhanced by wall-cooling effects in hypersonic TBLs. Zhang *et al.* (2022) reported that this enhancement originates from the generation of near-wall travelling-wave-like dilatational structures. To explore the features of wall pressure fluctuations beneath supersonic TBLs, Kistler & Chen (1963) performed the first measurement in the range of $1.33 \leq M \leq 5$. They reported that increasing M has the main effect of decreasing the characteristic length scale of the pressure-carrying eddies. Beresh *et al.* (2011) obtained fluctuating wall pressure signals up to $M = 3$ and compared the root-mean-square (r.m.s.) levels with a cluster of data from high-speed measurements. However, a large scatter was found in the data, primarily due to limitations in the frequency response of pressure sensors. Due to the advantage of being able to provide accurate three-dimensional global flow data, high-fidelity numerical simulations have been employed to study the characteristics of pressure fluctuations more recently. Duan, Beekman & Martín (2011) performed systematic direct numerical simulations (DNS) of TBLs with M ranging from 0.3 to 12, and reported that the compressibility effects are reflected by the increase in fluctuations of thermodynamic quantities and turbulent Mach numbers. Bernardini & Pirozzoli (2011) analysed the intensity, frequency spectrum, space–time correlation and convection velocity of pressure fluctuations by means of DNS at $M = 2, 3, 4$. The results showed that the increased intensities are mainly present near the wall and in the free stream, which are associated with enhanced genuine compressibility effects (reflected by dilatation fluctuations) and acoustic radiation, respectively. Focusing on comparing the characteristics of the free stream and wall pressure fluctuations, Duan, Choudhari & Wu (2014) observed important differences in aspects of amplitude, frequency

content and convection speeds. Subsequently, they continuously carried out a series of DNS on the corresponding situations in hypersonic TBLs. Based on the implicit large-eddy simulation (iLES), Ritos *et al.* (2019*a*); Ritos, Drikakis & Kokkinakis (2019*b*) investigated the wall pressure fluctuations beneath supersonic and hypersonic TBLs and proposed a modified spectrum model by introducing compressibility corrections. Gerolymos & Vallet (2023) constructed a (Re, M)-matrix database of compressible turbulent channel flow and summarized Mach number effects on pressure fluctuations based on turbulent statistics. Nonetheless, the underlying scaling relation between pressure fluctuations and Mach number from the perspective of flow physics, such as the generation mechanism of pressure fluctuations, necessitates further exploration.

The well-known classic spectrum model of wall pressure fluctuations, the Chase–Howe model (Chase 1980, 1987; Howe 1998), was developed to characterize the pressure fluctuations in weakly compressible flow, based on their generation mechanisms: mean flow–turbulence and turbulence–turbulence interactions. According to the terms specified in the governing Poisson equation for pressure fluctuations, as outlined in Pope (2000), these fluctuations can be theoretically decomposed into two primary components: rapid pressure (p_r) and slow pressure (p_s). These components are associated with the generation mechanisms of mean flow–turbulence and turbulence–turbulence interactions, respectively. In the context of arbitrary compressible flows, Sarkar (1992) derived the equation for pressure fluctuations and introduced a compressible pressure component (p_c) to account for compressibility effects. This component is utilized to estimate pressure–dilatation correlations by isolating a single contributing factor. Following this approach, Foysi, Sarkar & Friedrich (2004) extended the Poisson-equation-based pressure decomposition method to compressible channel flow, enabling the study of pressure–strain correlations in different components. Tang *et al.* (2020) and Yu *et al.* (2020) split the pressure fluctuations in compressible channel flow with relatively high Mach numbers and highlighted the significance of the genuine compressibility effects and compressible pressure component. Recently, Zhang *et al.* (2022) extended the pressure decomposition method and applied it to compressible TBLs to illustrate wall-cooling effects on pressure fluctuations from the perspective of generation mechanisms. Generally, the pressure decomposition method has been widely used to investigate the mechanism of pressure fluctuations, including the characteristics of pressure fluctuation sources (Chang, Piomelli & Blake 1999; Anantharamu & Mahesh 2020), pressure–strain correlation (Foysi *et al.* 2004), wall echo effects (Gerolymos, Sénéchal & Vallet 2013) and wall pressure spectrum (Hu, Reiche & Ewert 2017; Grasso *et al.* 2019; Yang & Yang 2022), and it becomes a viable approach to provide fruitful physical insight originating from the generation mechanisms of pressure fluctuations.

To correlate the distribution profiles of turbulent statistics properties scaled by wall units in incompressible and compressible wall-bounded turbulence, Morkovin (1962) hypothesized that when the turbulent Mach number is sufficiently small, compressible wall-bounded flows can be mapped onto the incompressible counterparts by taking the variation of mean properties (density, viscosity, etc.) into account. The Van Driest transform (Van Driest 1951) for mean velocity $\bar{u}$ and the resulting Morkovin scaling for velocity fluctuation $\boldsymbol{u}'_{rms}$ are widely used and even serve as a 'standard' when analysing compressible adiabatic wall-bounded turbulence. Concerning the diabatic one, especially with wall cooling, the Van Driest transform becomes less accurate. Recently, several improved transformations have been developed, such as the transformation of Trettel & Larsson (2016) in the semilocal scaling, the data-driven-based transformation of Volpiani *et al.* (2020) and the total-stress-based transformation of Griffin, Fu & Moin (2021).

These relations are not only of theoretical interest but also play an essential role in reduced-order turbulence modelling (Griffin, Fu & Moin 2023). However, the mapping onto incompressible flow becomes significantly distinct when considering pressure fields. Unlike the velocity field, which is primarily associated with the vorticity mode, the pressure field is intrinsically influenced by multiple modes, especially the vorticity and acoustic modes. As a result, establishing a mapping relation for pressure fluctuations inevitably poses greater challenges.

The scope of this study is to analyse DNS data of compressible TBLs in a relatively wide range of free stream Mach numbers from 0.5 to 8.0 and to investigate the relationship between pressure fluctuations and Mach numbers. In particular, the intrinsic scaling relation of pressure fluctuations is explored by analysing the components of pressure fluctuations from the perspective of generation mechanisms. Additionally, inspired by this intrinsic scaling relation, a semiempirical model predicting the dependence of pressure fluctuations on Mach number is proposed. The remainder of the paper is organized as follows. The numerical methods and simulation details are illustrated in § 2. The analysis of the components of pressure fluctuations and the scaling relation are discussed in § 3. The semiempirical model of pressure fluctuations is presented in § 3.4. The main findings and discussions are summarized in § 4.

2. The DNS of compressible TBL

Building on the insights gained from our prior studies (Zhang *et al.* 2022, 2023), DNS of five TBLs with a free stream Mach number range of $0.5 \leq M \leq 8.0$ are performed by solving the fully compressible Navier–Stokes equations for the compressible, viscous and ideal gas. The simulations are conducted based on the open-source code STREAmS (Bernardini *et al.* 2021), which can be efficiently accelerated by graphics processing units. The coefficient of viscosity μ is set as a function of temperature according to Sutherland's law. The equations are solved in a stretched Cartesian coordinate system and discretized by high-order finite-difference methods. The spatial discretization of the convective term adopts a hybrid energy-preserving–shock-capturing scheme in a locally conservative form. The convective flux is calculated by the eighth-order energy-preserving scheme (Pirozzoli 2010) in smooth (shock-free) regions of the flow. Otherwise, in discontinuous regions, the Lax–Friedrichs flux vector splitting ensures robust shock-capturing capabilities with the characteristic fluxes at interfaces reconstructed by the seventh-order weighted essentially non-oscillatory scheme (Jiang & Shu 1996). To avoid odd–even decoupling phenomena, the viscous terms are expanded to Laplacian form and approximated by the sixth-order central finite-difference formula. The assembled semidiscrete system is advanced in time by a three-stage, third-order Runge–Kutta scheme (Spalart, Moser & Rogers 1991). More details of the numerical methods can be found in the original paper introducing this solver (Bernardini *et al.* 2021).

The schematic of the computational model used for a plate TBL is illustrated in figure 1. The inflow condition is established through the recycling–rescaling scheme (Pirozzoli, Bernardini & Grasso 2010) to attain a fully developed turbulent state. This approach introduces less numerical noise into the flow field than a synthetic inflow like the conventional digital filtering method (Ceci *et al.* 2022). At the upper and outflow boundaries, non-reflecting boundary conditions (Poinsot & Lele 1992) are imposed according to the characteristic decomposition in the direction normal to the boundary. At the no-slip isothermal wall boundary, the wall temperature is set equal to the recovery temperature $T_r = T_\infty(1 + r(\gamma - 1)M^2/2)$ based on a recovery factor of $r = 0.89$, and a similar characteristic wave treatment is also applied. Hyperbolic sine stretching is applied

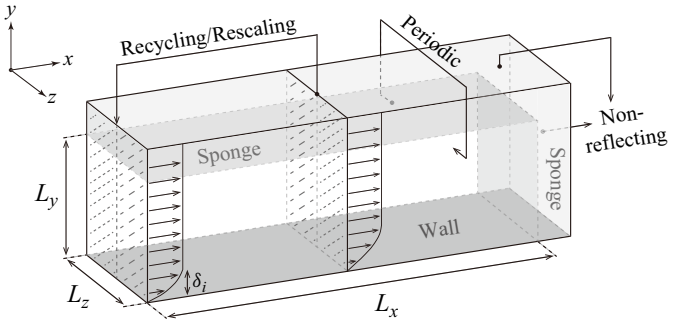

Figure 1. Schematic of the computational model (not in scale). The computational physical domain is surrounded by the sponge zones at the top and tail.

in the wall-normal direction to ensure sufficient resolution near the wall, and uniform grid spacing is adopted in the wall-parallel directions except in the sponge zone (Adams 1998), which is added surrounding the computational physical domain at the top and tail to further eliminate non-physical reflections. For the spanwise direction, a periodic boundary condition is applied. Table 1 shows the DNS parameters of the present computational cases. Five compressible TBLs with free stream Mach numbers M ranging from 0.5 to 8 are solved. Compared with other reliable DNS of compressible TBLs (Zhang *et al.* 2017; Bernardini *et al.* 2021; Huang, Duan & Choudhari 2022; Xu, Wang & Chen 2022), the grid resolutions used have met the requirements of DNS, with the current grid size of each case exceeding 460×10^6. Moreover, higher grid resolutions are achieved in the two hypersonic TBLs to capture finer turbulent structures. The typical first- and second-order flow statistics have been validated by matching reference data in our previous work (Zhang *et al.* 2022), verifying the reliability of current data.

Table 2 illustrates the statistical properties of TBLs at the station selected for analysis. All cases are analysed under approximately the same friction Reynolds numbers of $Re_\tau \approx 630$, while the Reynolds numbers based on boundary layer thickness Re_δ and based on momentum thickness Re_θ and Re_{δ_2} increase monotonically with increasing M. In the case of adiabatic-wall TBLs, previous studies (Bernardini & Pirozzoli 2011; Zhang *et al.* 2017; Gerolymos & Vallet 2023) have demonstrated that standard wall units perform quite well in scaling pressure fluctuations, and thus we here attempt to find the potential scaling relationship between pressure fluctuations and M by fixing Re_τ. Similarly, friction factor C_f and wall pressure fluctuation intensity in wall-unit $p'_{rms,w}/\tau_w$ are also of monotonic behaviour with increasing M, where the monotonic increase of $p'_{rms,w}/\tau_w$ is attributed to the enhancement of compressibility. In this study, thermodynamics variables are decomposed using the standard Reynolds decomposition $f = \bar{f} + f'$ and the velocity variables are decomposed using density-weighted (Favre) representation $f = \tilde{f} + f''$, where $\tilde{f} = \overline{\rho f}/\bar{\rho}$. The superscript $(\bullet)^+$ denotes the variable normalized by the wall unit. The subscripts $(\bullet)_w$ and $(\bullet)_\infty$ denote the variables at the wall and in free stream, respectively.

3. Scaling relations of pressure fluctuations with Mach number

In this section, some inspiring insights into vorticity and acoustic modes are obtained from the statistical characteristics of representative quantities. Then, the direct scaling relations of original pressure fluctuations with M are examined. Lastly, we investigate the intrinsic

https://doi.org/10.1017/jfm.2024.566 Published online by Cambridge University Press

Cases	M	$N_x \times N_y \times N_z$	$L_x \times L_y \times L_z$	Δx^+	Δy_w^+	Δy_e^+	$\Delta y_e^\star$	Δz^+	N_f	$t_s u_\infty/\delta_i$
M0	0.5	$2400 \times 320 \times 600$	$67.1\delta_i \times 8.0\delta_i \times 10.5\delta_i$	9.4	0.76	9.6	10.0	5.7	201	260.0
M2	2.0	$2400 \times 320 \times 600$	$67.8\delta_i \times 8.2\delta_i \times 10.6\delta_i$	12.1	0.77	10.5	24.4	7.2	210	584.6
M4	4.0	$2400 \times 320 \times 600$	$46.6\delta_i \times 8.6\delta_i \times 8.5\delta_i$	9.2	0.77	10.8	81.0	6.4	360	1550.0
M6	6.0	$2400 \times 320 \times 600$	$48.0\delta_i \times 7.9\delta_i \times 6.3\delta_i$	9.0	0.57	11.0	352.4	4.5	243	702.6
M8	8.0	$3600 \times 320 \times 400$	$50.2\delta_i \times 7.0\delta_i \times 5.1\delta_i$	6.2	0.46	11.0	763.2	5.5	235	231.1

Table 1. The simulation parameters for different cases: M is the free stream Mach number; N and L are the number of grid points and the length of the physical computational domain, respectively; Δx^+ and Δz^+ represent the non-dimensional grid spacings in the wall unit of streamwise and spanwise directions; Δy_w^+ and Δy_e^+ represent the wall-normal grid spacings at the wall and at the boundary edge, respectively; $\Delta y_e^\star$ represents the wall-normal grid spacings at the boundary edge in the semilocal scale; N_f is the number of flow fields for statistics; $t_s u_\infty/\delta_i$ is the time period for statistics.

Cases	x_a/δ_i	Re_τ	$Re^\star_\tau$	Re_δ	Re_θ	Re_{δ_2}	$T_\infty(K)$	$C_f \times 10^3$	$p'_{rms,w}/\tau_w$
M0	49.6	628	664	15 394	1626	1572	298	3.71	2.58
M2	35.4	650	1301	35 933	2898	1907	220	2.59	2.88
M4	30.4	649	3322	127 095	6324	2426	220	1.37	2.92
M6	37.6	632	11 098	560 476	18 860	2930	55	0.78	2.95
M8	40.9	623	20 111	1 342 856	33 603	3578	51.8	0.48	3.00

Table 2. Parameters of the TBL: x_a denotes the streamwise location for analysis. The friction Reynolds number and semilocal friction Reynolds number are $Re_\tau = \rho_w u_\tau \delta/\mu_w$ and $Re^\star_\tau = (\rho_\infty \tau_w)^{1/2}\delta/\mu_\infty$, where δ is the boundary layer thickness. The Reynolds number based on boundary layer thickness is $Re_\delta = \rho_\infty u_\infty \delta/\mu_\infty$. The Reynolds numbers based on momentum thickness are $Re_\theta = \rho_\infty u_\infty \theta/\mu_\infty$ and $Re_{\delta_2} = \rho_\infty u_\infty \theta/\mu_w$. Here T_∞ is the free stream temperature; $C_f = 2\tau_w/\rho_\infty u^2_\infty$ is the friction factor; $p'_{rms,w}/\tau_w$ means the non-dimensional wall pressure fluctuation intensity in the wall unit.

scaling relations embedded within the generation mechanisms of pressure fluctuations, employing the pressure decomposition method.

3.1. *The turbulent statistics for vorticity and acoustic modes*

For velocity fields dominated by the vorticity mode, figure 2 presents the first- and second-moment statistics of the streamwise velocity. As shown in figure 2(*a*), the profiles of mean velocity $\bar{u}^+$ for all cases reasonably agree with the wall law in the range of $y^+ < 5$, but only the distribution for case M0 exhibits a good agreement with the log law where compressibility is negligibly weak. With increasing M, the profiles gradually deviate from the log law. After considering variations in mean density in figure 2(*b*), it is observed that the profiles of Van Driest transformed (Van Driest 1951) mean velocity $\bar{u}_{vd}$ for all cases agree well with each other in both near-wall and log-law regions. Similarly, for velocity fluctuations intensities u'^+_{rms} in figure 2(*c*), only the profile of case M0 collapses with the incompressible profile (Jiménez *et al.* 2010), while the profiles of other cases with higher M gradually deviate from the incompressible profile. Following the relations of strong Reynolds analogy (Morkovin 1962), when the variation of mean density is taken into account, it can be seen in figure 2(*d*) that the profiles of density-scaled fluctuation intensities exhibit superior clustering and collapse compared with those of u'^+_{rms}. The obtained results not only validate the accuracy of the present data but also demonstrate the efficacy of utilizing Morkovin's hypothesis to map the statistics of compressible velocity fields onto their incompressible counterparts.

Considering that pressure fluctuations in compressible TBLs are mainly influenced by both the vorticity mode and acoustic mode (Phillips 1960; Lilley 1963), figure 3 presents the profiles of vorticity fluctuation intensities ω'^+_{rms} and dilatation fluctuation intensities θ'^+_{rms}, which can characterize the vorticity mode and acoustic mode to a certain extent, respectively. As shown in figure 3(*a*), the profiles of ω'^+_{rms} for all cases collapse well with each other at the fixed Re_τ, indicating that the profiles of ω'^+_{rms} are almost not affected by increasing M. The magnitude of the vorticity mode seems to be controlled only by the parameter of Re_τ. For dilatation fluctuations, the increase in M monotonically enhances θ'^+_{rms} especially near the wall, as shown in figure 3(*b*). The magnitude of θ'^+_{rms} gradually weakens as the wall-normal position moves away from the wall. The distribution trends of ω'^+_{rms} and θ'^+_{rms} are consistent with the DNS data reported by Bernardini & Pirozzoli (2011). These findings imply the presence of intrinsic scaling relations, particularly when the vorticity and acoustic modes are properly isolated. Specifically, the contribution of the

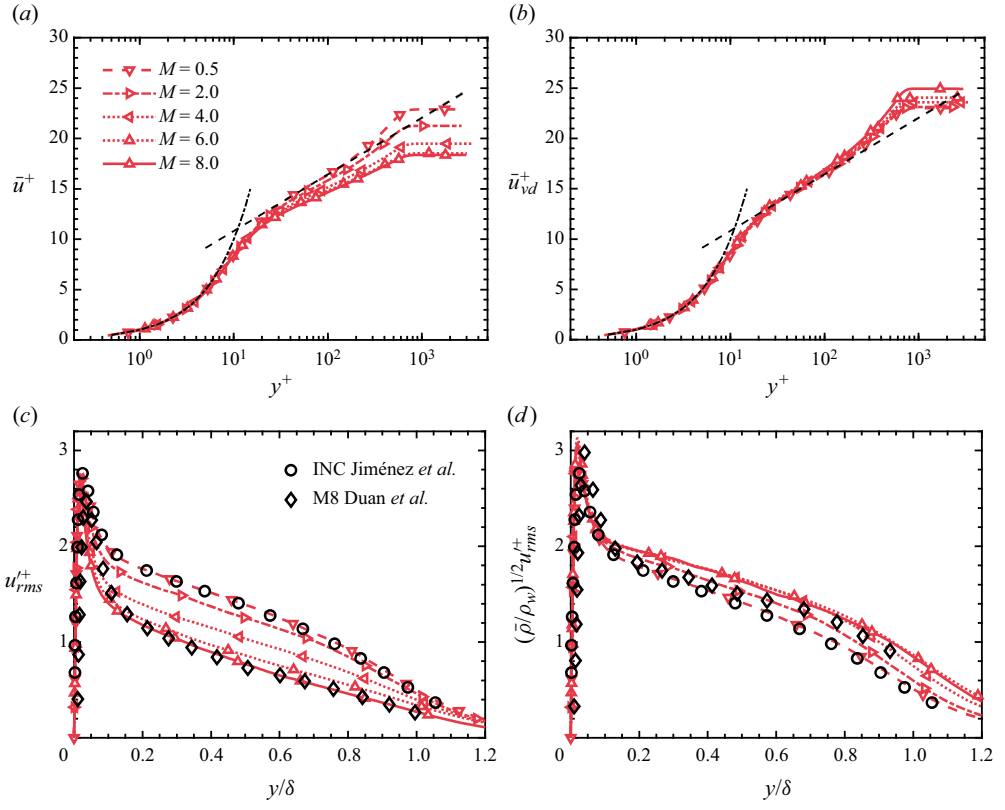

Figure 2. Statistical properties of streamwise velocity: (*a*) mean velocity $\bar{u}^+$; (*b*) Van Driest transformed mean velocity $\bar{u}^+_{vd}$; (*c*) fluctuation intensity; (*d*) density scaled fluctuation intensity. The dot–dashed and dashed lines denote the wall law $u^+ = y^+$ and the log law $u^+ = \log(y^+)/0.41 + 5.2$, respectively. The circles indicate the reference data of an incompressible TBL with $Re_\tau = 580$ from Jiménez *et al.* (2010). The diamonds denote a $M = 8$ TBL with $Re_\tau = 398$ from Duan *et al.* (2011).

vorticity mode to pressure fluctuations is independent of M, while the contribution of the acoustic mode exhibits a monotonic increase with M.

3.2. *The direct scaling relations of pressure fluctuations*

To illustrate the scaling relations between pressure fluctuations and M directly, figure 4 shows the profiles of pressure fluctuation intensities p'^+_{rms} in both the outer and inner scales, respectively. The profiles of all cases exhibit a similar trend that p'^+_{rms} increases from its value at the wall and reaches the global maximum at $y^+ \approx 12$ and then gradually decays to a plateau value out of the boundary layer where acoustic radiations dominate. As indicated by the black arrow in figure 4(*a*), the increase in M overall enhances p'^+_{rms} monotonically, corresponding to stronger acoustic modes in cases of higher M. The profile of the M0 case closely aligns with the reference data of an incompressible TBL (Jiménez *et al.* 2010). Within the boundary layer, the near-wall enhancement clearly shown in figure 4(*b*) is a consequence of the stronger genuine compressibility in higher-M cases, as demonstrated by θ'^+_{rms} in figure 3(*b*). In the far field, the enhancement in supersonic and hypersonic cases should be attributed to the Mach-wave radiation, which is induced by the supersonic convection eddies within TBLs. Because of the comprehensive contributions

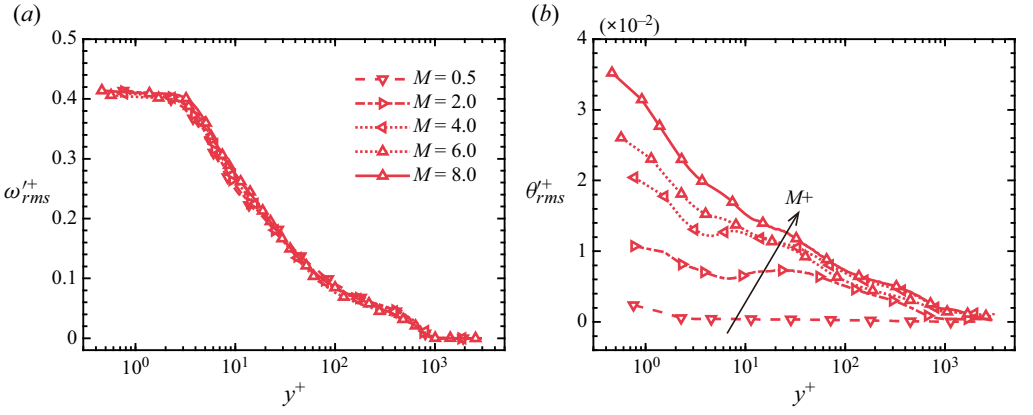

Figure 3. (*a*) Vorticity fluctuation intensities ω'^{+}_{rms} and (*b*) dilatation fluctuation intensities θ'^{+}_{rms}.

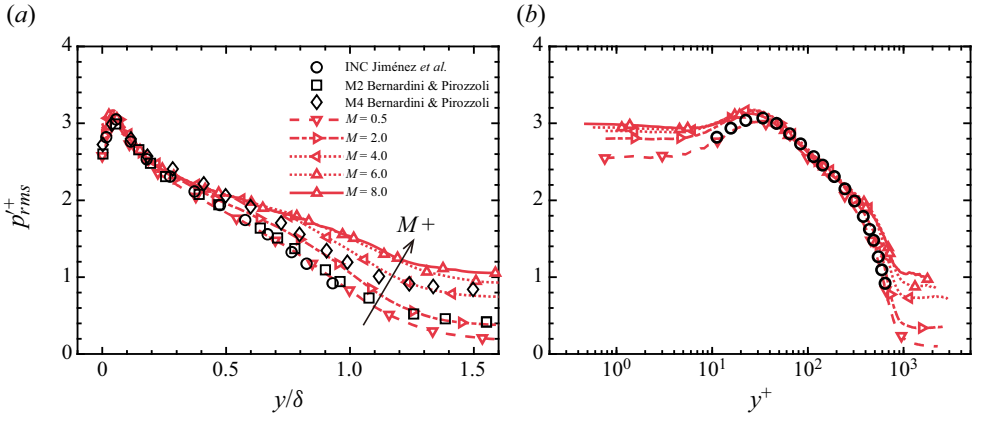

Figure 4. Intensities of pressure fluctuations p'^{+}_{rms} shown in (*a*) the outer scale and (*b*) the inner scale. The circles indicate the reference data of an incompressible TBL with $Re_\tau = 690$ from Jiménez *et al.* (2010). The squares and diamonds denote $M = 2$ and 4 TBLs with $Re_\tau = 508$ and 506, respectively, from Bernardini & Pirozzoli (2011).

from the vorticity and acoustic modes, considering the variations in mean quantities may not be a viable solution when mapping the compressible profile of pressure fluctuations to the incompressible counterpart. Instead, removing the contribution of acoustic modes to pressure fluctuations is expected to work.

For evaluating the scaling relations of wall and far-field pressure fluctuations, the variations of pressure fluctuation intensities versus M are shown in figure 5. For wall pressure fluctuation intensities normalized by the free stream dynamic pressure p'_{rms}/q_∞, the data from measurements (grey square), simulations (red symbols) and prediction models (dashed lines) are collected in figure 5(*a*). Due to the limitations of pressure sensors in experiments, from light to dark colours, the grey squares indicate the uncorrected raw data, the corrected data by Corcos corrections (Corcos 1963) and the extended data further corrected based on an estimation of high-frequency spectra. It is shown that the corrected experimental data agree much better with simulation data than the original data. For compressible flows, Laganelli, Martellucci & Shaw (1983) proposed an

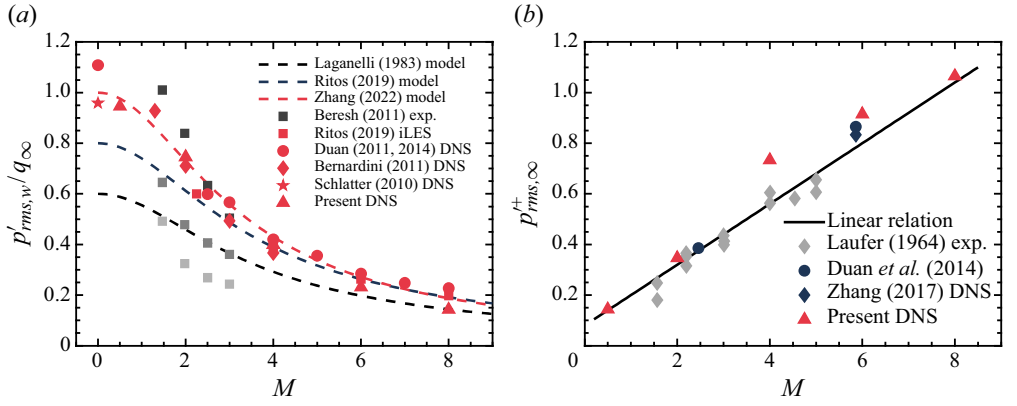

Figure 5. Pressure fluctuation intensities with scaling models (*a*) at the wall and (*b*) in the far-field.

empirical model by extending an incompressible theory to compressible states, written as

$$p'_{rms,w}/q_\infty = \frac{\sigma}{\left[0.5 + (T_w/T_r)\left(0.5 + 0.09M^2\right) + 0.04M^2\right]^\phi}, \tag{3.1}$$

where the two parameters σ and ϕ are determined by fitting experimental data. Their original values are $\sigma = 0.006$ and $\phi = 0.64$. Considering the potential bias in historical experimental data, the predictions of the original Laganelli model exhibit an overall underestimation compared with the numerical data. Therefore, Ritos *et al.* (2019*a*) improved the model by introducing a modified $\sigma = 0.008$ based on fitting their iLES data in a range of $2.25 \leq M \leq 8$, but significant deviations still occur at the relatively lower Mach number range of $M < 2$. By optimizing both two parameters, the modified model with $\sigma = 0.01$ and $\phi = 0.75$ proposed by Zhang *et al.* (2022) shows good performances in a wide Mach number range of $0 \leq M \leq 8$. Pressure fluctuation intensities normalized by the wall unit ($p'^{+}_{rms,\infty}$) in the far-field are also presented in figure 5(*b*), where grey diamonds indicate experimental data, red and blue symbols indicate numerical data with quasiadiabatic and cooled walls, respectively. The distributions of $p'^{+}_{rms,\infty}$ show approximately monotonic linear growths with increasing M. Consequently, a simple linear relation expressed as $p'^{+}_{rms,\infty} = 0.12M + 0.08$, can be obtained by fitting these data.

3.3. *The intrinsic scaling relations of decomposed pressure components*

In an effort to discern the respective contributions of vorticity and acoustic modes from the perspective of the generation mechanism of pressure fluctuations, we employ a decomposition method based on the governing equation of pressure fluctuations. This approach enables us to investigate the intrinsic scaling relations. Starting from the governing equations for mass and momentum in a Cartesian coordinate system written as

$$\frac{\partial \rho}{\partial t} + \frac{\partial \rho u_j}{\partial x_j} = 0, \tag{3.2}$$

$$\frac{\partial \rho u_i}{\partial t} + \frac{\partial \rho u_i u_j}{\partial x_j} = -\frac{\partial p}{\partial x_i} + \frac{\partial \tau_{ij}}{\partial x_j}, \tag{3.3}$$

where τ_{ij} is the viscous stress tensor, take the divergence of the momentum equations (3.3) yielding

$$\frac{\partial^2 p}{\partial x_i \partial x_i} = -\frac{\partial^2}{\partial x_i \partial x_j}\left(\rho u_i u_j - \tau_{ij}\right) - \frac{\partial}{\partial x_i}\frac{\partial \rho u_i}{\partial t}. \tag{3.4}$$

By subtracting the average of (3.4) from itself and combining the continuity equation (equation (3.2)), the governing equation of pressure fluctuations can be written as (Gerolymos, Sénéchal & Vallet 2007)

$$\frac{\partial^2 p'}{\partial x_i \partial x_i} = \frac{\partial^2}{\partial x_i \partial x_j}\tau'_{ij} - \frac{\partial^2}{\partial x_i \partial x_j}\left(2\rho \tilde{u}_i u''_j + \rho' \tilde{u}_i \tilde{u}_j\right) - \frac{\partial^2}{\partial x_i \partial x_j}\left(\rho u''_i u''_j - \overline{\rho u''_i u''_j}\right) + \frac{\partial^2 \rho'}{\partial t^2}. \tag{3.5}$$

According to characteristics of the source terms on the right-hand side of (3.5), the pressure fluctuation can be decomposed into several components (Yu *et al.* 2020; Zhang *et al.* 2022), $p' = p_r + p_s + p_\tau + p_c + p_h$. These components individually satisfy

$$\frac{\partial^2 p_r}{\partial x_i \partial x_i} = -2\frac{\partial \tilde{u}_i}{\partial x_j}\frac{\partial \rho u''_j}{\partial x_i}, \tag{3.6a}$$

$$\frac{\partial^2 p_s}{\partial x_i \partial x_i} = -\frac{\partial^2}{\partial x_i \partial x_j}\left(\rho u''_i u''_j - \overline{\rho u''_i u''_j}\right), \tag{3.6b}$$

$$\frac{\partial^2 p_\tau}{\partial x_i \partial x_i} = \frac{\partial^2 \tau'_{ij}}{\partial x_i \partial x_j}, \tag{3.6c}$$

$$\frac{\partial^2 p_c}{\partial x_i \partial x_i} = \frac{\partial^2 \rho'}{\partial t^2} - \frac{\partial^2}{\partial x_i \partial x_j}\left(2\rho \tilde{u}_i u''_j + \rho' \tilde{u}_i \tilde{u}_j\right) + 2\frac{\partial \tilde{u}_i}{\partial x_j}\frac{\partial \rho u''_j}{\partial x_i}, \tag{3.6d}$$

$$\frac{\partial^2 p_h}{\partial x_i \partial x_i} = 0, \tag{3.6e}$$

where the first two components p_r and p_s are so-called rapid and slow pressures similar to those in incompressible flow, caused by linear mean flow–turbulence interactions and nonlinear turbulence–turbulence interactions, respectively; the viscous pressure p_τ corresponds to the contribution of the viscous stress; the compressible pressure p_c accounts for contributions of compressibility which is the principal representation of the essential nature of compressibility effects on the pressure statistics (Sarkar 1992; Foysi *et al.* 2004; Tang *et al.* 2020); and the harmonic pressure p_h is introduced to denote the contribution of streamwise boundary conditions (Pope 2000). All the right-hand side source terms are obtained by discretization based on the DNS data. The Poisson equations of pressure components are solved by the Fourier–Galerkin scheme in a subdomain of the computational domain as shown in figure 6 with the specific boundary conditions given in table 3. The grid of the subdomain is the same as that of the DNS computation but truncated in the streamwise and wall-normal directions. In the streamwise direction, the subdomain spans over 800 points for all cases except case M8, which increases to 1200 points due to its smaller grid spacing. The location for analysis is at the streamwise midpoint of the subdomain. In the wall-normal direction, the subdomain spans over 280 points starting from the wall, and the wall-normal location of the upper boundary exceeds 3δ ensuring acoustic radiation dominants here. Note that due to the evanescent nature of vortex waves and entropy waves out of boundary layers, other pressure components except

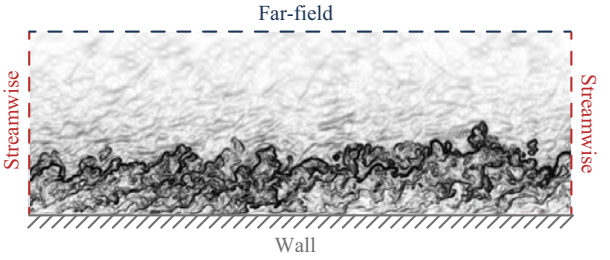

Figure 6. Schematic for the pressure decomposition. The subdomain of the numerical schlieren of the M8 case is drawn.

Boundary conditions	p_r	p_s	p_τ	p_c	p_h
Streamwise	$\partial p_r/\partial x = 0$	$\partial p_s/\partial x = 0$	$\partial p_\tau/\partial x = 0$	$\partial p_c/\partial x = 0$	$\partial p_h/\partial x = \partial p'/\partial x$
Wall	$\partial p_r/\partial y = 0$	$\partial p_s/\partial y = 0$	$\partial p_\tau/\partial y = 0$	$\partial p_c/\partial y = 0$	$\partial p_h/\partial y = \partial p'/\partial y$
Far-field	$p_r = 0$	$p_s = 0$	$p_\tau = 0$	$p_c = p'$	$p_h = 0$

Table 3. Boundary conditions of the pressure fluctuation equations for each pressure component.

p_c are set to 0 at the far-field boundary, while the propagation nature of acoustic waves is mainly reflected in the compressible pressure p_c, so that $p_c = p'$ is imposed at the far-field.

According to generation mechanisms of pressure fluctuations from the characteristics of the source terms, the compressible pressure p_c is used to represent the contributions from the acoustic mode. Meanwhile, the sum of the remaining components, $p_i = p_r + p_s + p_\tau + p_h$, is nominally defined as the hydrodynamic pressure (quasi-incompressible component) denoting the contributions from the vorticity mode, resulting in $p' = p_i + p_c$. The instantaneous fields of the original pressure fluctuations p'^+ as well as the compressible pressure p_c^+ and hydrodynamic pressure p_i^+ in wall scaling are depicted in figure 7, taking the M0, M2 and M8 cases as examples for brevity. For p'^+ fields in figure 7(*a*,*b*), pressure fluctuations are mainly associated with vortex structures within the boundary layer. In the far field, pressure fluctuations radiate as acoustic waves, which are relatively weak in case M0. As the Mach number increases, the amplitudes of radiating pressure fluctuations in the far field become higher. In case M8 depicted in figure 7(*c*), radiating pressure fluctuations are comparable to those within the boundary layer. For p_i^+ shown in figure 7(*d–f*), the same feature of all cases is that all fluctuations seem to be bounded within the boundary layer and rapidly decay to zero out of the boundary layer. The amplitudes of p_i^+ are comparable to those of p'^+ fields for each case. The distributions of p_i^+ within boundary layers are very similar to those of p'^+, except for case M8, in which the acoustic mode becomes much stronger. It can be noted that there are no discernible distinctions in the p_i^+ field among these three cases. The patterns observed in the spanwise planes are reminiscent of the inclined convective vortex structures depicted in figure 6. For p_c^+ fields in figure 7(*g*,*h*), the characteristics are quite different in that the fluctuations occupy the whole domain, and the acoustic radiations out of the boundary layers are well captured. As M increases, the amplitude and characteristic length scales of p_c^+ gradually become higher and finer, respectively. For case M0, the fluctuation of p_c^+ is quite weak, and its amplitude is an order lower than that of p_i^+. The acoustic waves in the streamwise and spanwise planes are shown to be of large wavelengths, aligning with the large-scale patchy patterns at the wall. For case M2, the patchy patterns at the wall become finer, and

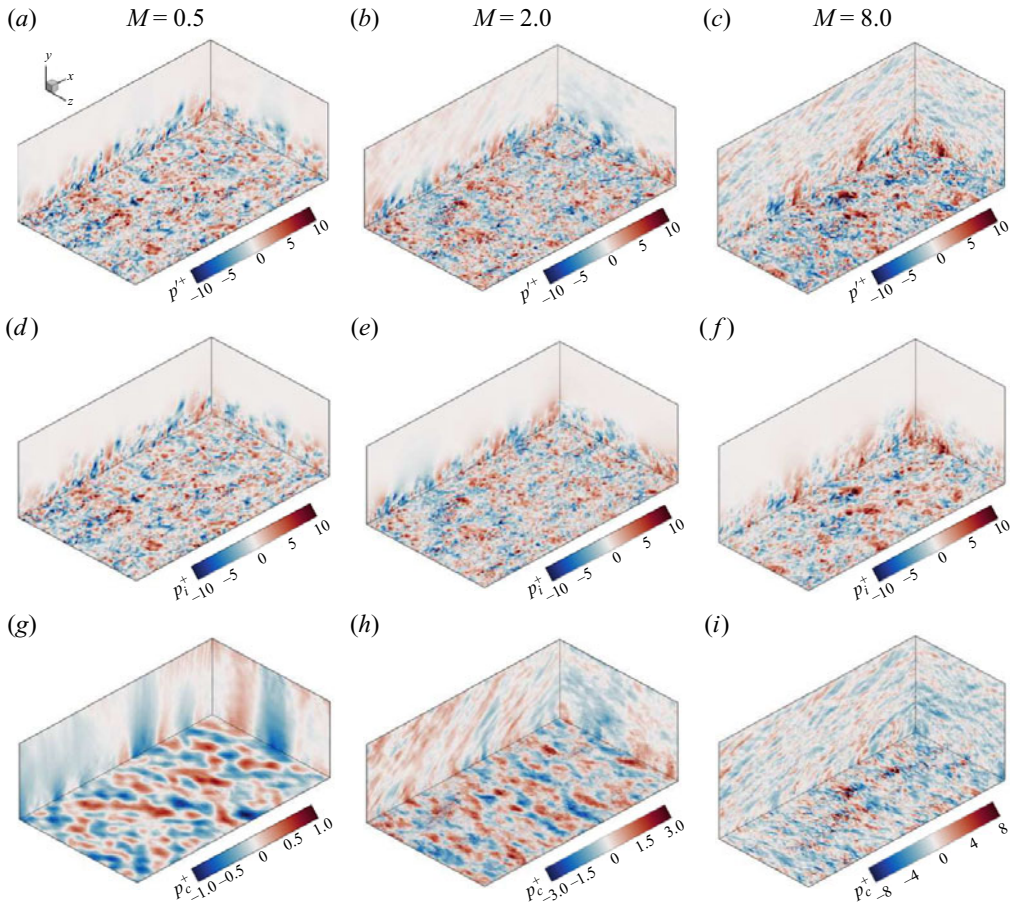

Figure 7. The instantaneous fields of (*a–c*) the pressure fluctuation p'^{+} (*d–f*) the hydrodynamic pressure p_i^{+} and (*g–i*) the compressible pressure p_c^{+}. The spanwise, streamwise and wall planes are shown.

the acoustic waves out of the boundary layer are inclined due to the Doppler effect. In case M8, the amplitudes of p_c^{+} are much higher and comparable to those of p'^{+}, and the distributions are very similar to those of p'^{+}, suggesting the critical role of p_c^{+} in both the near and far fields for high Mach number cases.

Given the distinct convection velocities of vorticity and acoustic modes, space–time correlation functions are computed to assess and quantify this characteristic feature, written as

$$R_p(\Delta \boldsymbol{x}, \Delta t) = \langle p(\boldsymbol{x}, t) p(\boldsymbol{x} + \Delta \boldsymbol{x}, t + \Delta t) \rangle \,. \tag{3.7}$$

For the boundary layer growing slowly in the limited analysis domain, the field can be treated as a homogeneous field. Thus, the function R_p is independent of $\boldsymbol{x}$ and t at the wall. Here, only the streamwise separation Δx is considered. As shown in figure 8(*a*), the normalized correlation functions of original wall pressure $R_{p'}$ gradually decay to zero with Δx and Δt increasing, forming contours with elongated shapes. The convection velocity u_c can be approximated by the slope of the line along which $R_{p'}$ decay most slowly. Across all cases, $u_c \approx 0.6 u_\infty$ at small time delay Δt, and u_c slightly increases when Δt becomes larger, aligning with the findings of Bernardini & Pirozzoli (2011) and Gloerfelt & Berland (2013). This behaviour is attributed to the slower movement of small-scale

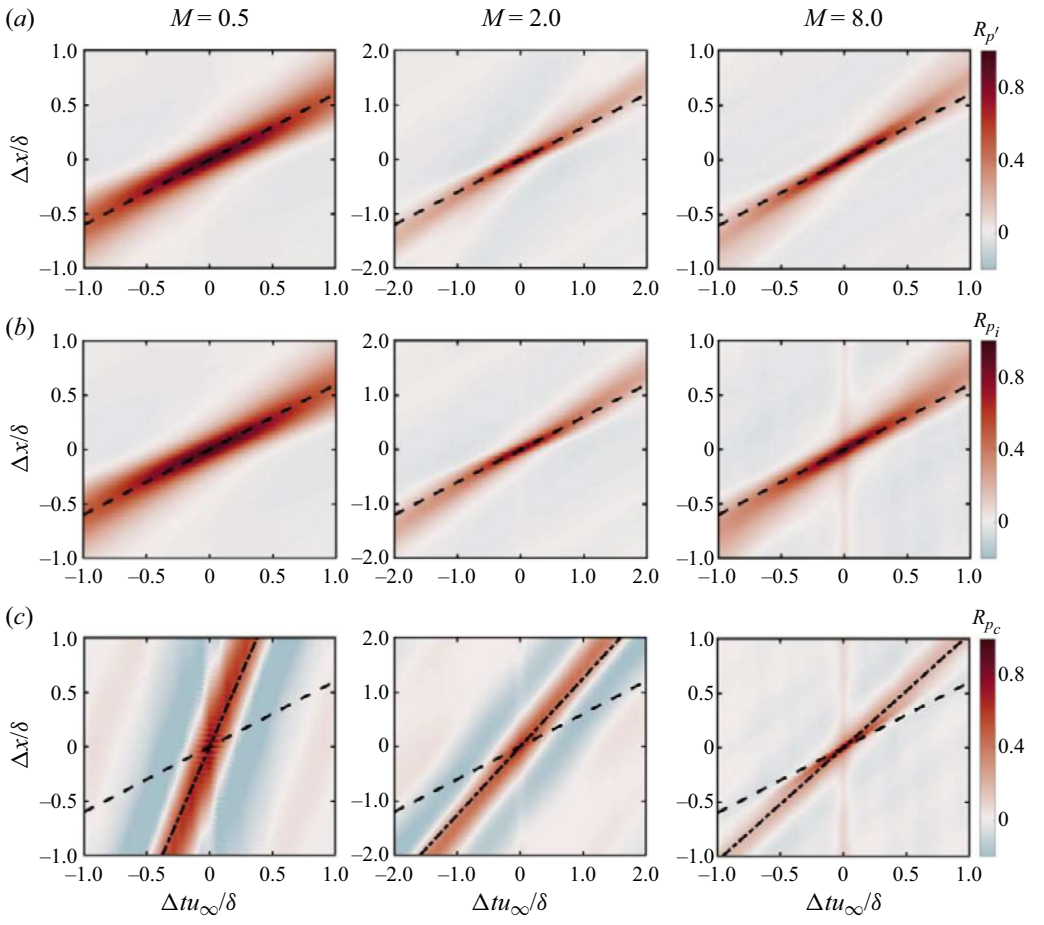

Figure 8. The normalized space–time correlation functions of wall pressure fluctuations for the (*a*) original pressure p'_w, (*b*) hydrodynamic pressure $p_{i,w}$ and (*c*) compressible pressure $p_{c,w}$. Slopes of the reference lines: – – –, $0.6u_\infty$; –·– ·–, $0.6u_\infty + a_w$ with a_w denoting the acoustic velocity at the wall.

turbulent structures near the wall and *vice versa* for larger-scale structures. In figure 8(*b*), the distributions of R_{p_i} closely resemble those of $R_{p'}$ with almost identical u_c, indicating the dominant role of the vorticity mode. For correlation functions of compressible pressure R_{p_c}, the convection velocity differs significantly, with an increase in the acoustic velocity at the wall, denoted as a_w, resulting in $u_c = 0.6u_\infty + a_w$. Moreover, the contour shape also becomes parallel strips with two negative strips flanking both sides. These features are reminiscent of wavefronts and are quite consistent with the propagation nature of acoustic waves. The narrow streak with a small value around $\Delta t = 0$ results from the harmonic pressure p_h for $M = 8$ case. Although the flow is highly nonlinear and the modes are strongly coupled with each other, the contributions from the acoustic mode and vorticity mode can be reasonably distinguished by utilizing the pressure decomposition method, based on the distinct characteristics of the p_i^+ and p_c^+ fields.

Drawing inspiration from the observed scaled relationships of vorticity and dilatation fluctuations in figure 3, it is anticipated that similar scaling laws may exist for pressure fluctuations concerning the vorticity and acoustic modes, which are nominally denoted by hydrodynamic pressure p_i^+ and compressible pressure p_c^+, respectively. As shown

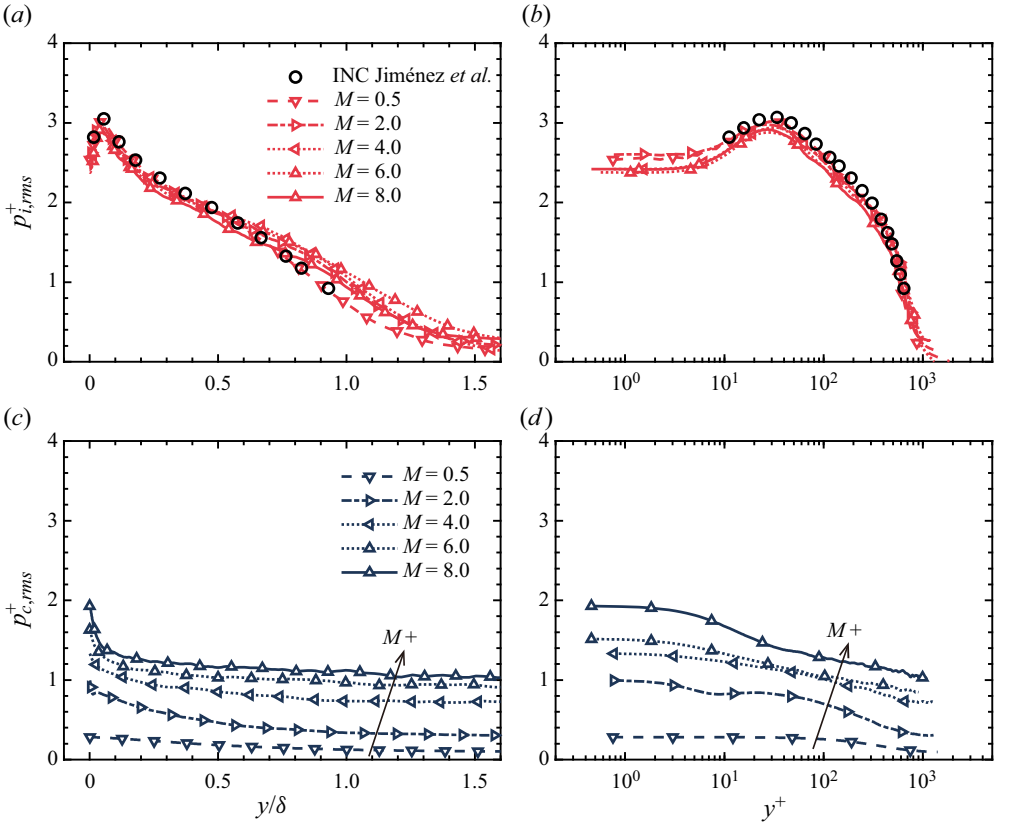

Figure 9. Pressure component fluctuation intensities in (*a*,*c*) the outer scale and (*b*,*d*) the inner scale: (*a*,*b*) hydrodynamic pressure $p^+_{i,rms}$, (*c*,*d*) compressible pressure $p^+_{c,rms}$. The circles indicate the reference data of an incompressible TBL with $Re_\tau = 690$ from Jiménez *et al.* (2010).

in figure 9(*a*,*b*), the profiles of fluctuation intensities of hydrodynamic pressure $p^+_{i,rms}$ exhibit uniform behaviour and collapse well with each other, including the profile of the incompressible TBL with a similar Reynolds number $Re_\tau = 690$ (Jiménez *et al.* 2010). These profiles share the same evolution trend along the wall-normal direction as the original pressure fluctuations depicted in figure 4, but they gradually diminish towards zero beyond the boundary layer, rather than reaching a plateau. This suggests that there exists a uniform intrinsic scaling wherein the distributions of $p^+_{i,rms}$ are in agreement with those of incompressible TBLs and are independent of Mach numbers without taking into account the possible effects of Reynolds number.

For compressible pressure $p^+_{c,rms}$ shown in figure 9(*c*,*d*), it is also found that the profiles exhibit a clear trend. With increasing M, $p^+_{c,rms}$ is monotonically enhanced and then decays to plateau values as the distance to the wall increases. The plateau values are also proportional to M. This relationship is in qualitative agreement with that of dilatation fluctuation intensities θ'^+_{rms} in figure 3(*b*), implying that the enhancement of p'^+_{rms} near the wall is mainly attributed to the increased genuine compressibility denoted by θ'^+_{rms}. In short, the profiles of pressure fluctuation intensities in compressible TBLs can be mapped onto their counterparts in incompressible TBLs if we physically remove the contribution from the acoustic mode.

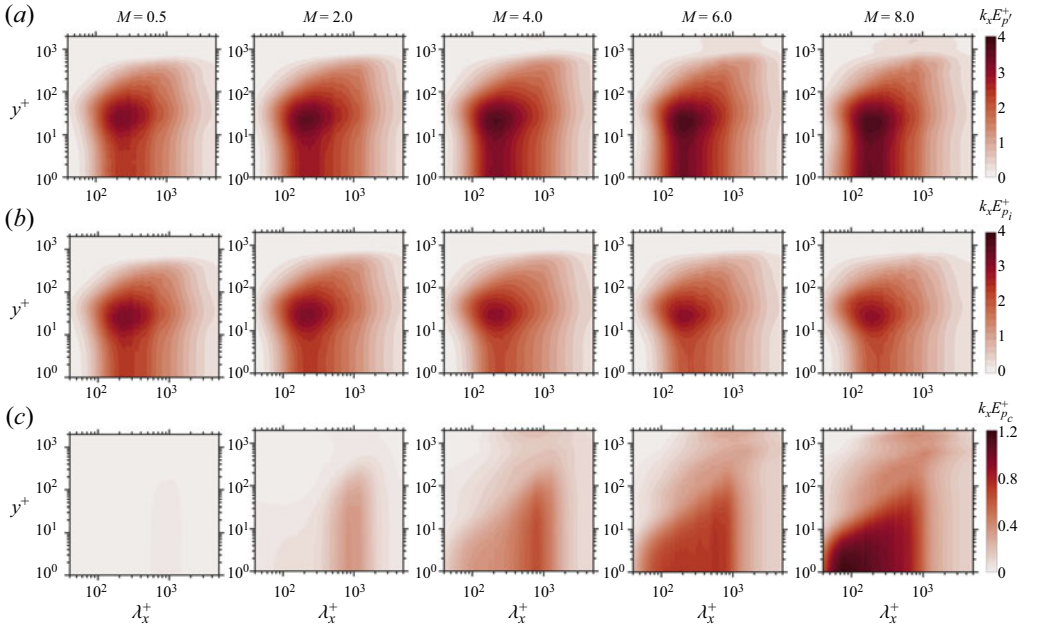

Figure 10. Premultiplied streamwise wavenumber spectra $k_x E_p^+$ of the (*a*) original pressure p', (*b*) hydrodynamic pressure p_i and (*c*) compressible pressure p_c.

To examine the characteristics of pressure components in the wavenumber space, the premultiplied streamwise wavenumber spectra are calculated. As M increases, the spectra of original pressure $k_x E_{p'}^+$ shown in figure 10(*a*) are overall enhanced. Notably, this enhancement is more pronounced in both the lower left-hand region (near the wall and short wavelength) and the upper right-hand region (outside the boundary layer and long wavelength). These enhancements are attributed to the presence of stronger near-wall small-scale structures and increased acoustic radiation, respectively. For the spectra of hydrodynamic pressure $k_x E_{p_i}^+$ in figure 10(*b*), the distributions are very similar for all cases including the contour shape and peak position. Due to the feature of the vorticity mode, there is no amplitude out of the boundary layer. The variations in $k_x E_{p'}^+$ can be clearly reflected by the contours of $k_x E_{p_c}^+$ in figure 10(*c*). For the three subsonic and supersonic cases, $k_x E_{p_c}^+$ manifests a dominant wavelength of $\lambda_x \sim \delta$, which persists up to the log layer. For the two hypersonic cases, the dominant wavelength shifts to be shorter $\lambda_x^+ \sim 100$, confined primarily within the buffer layer. This is because the near-wall small-scale dilatational structures are induced by strong compressibility (Zhang *et al.* 2022). Hence, the intrinsic behaviour of p_i and monotonic enhancing feature of p_c also exist in the wavenumber space.

3.4. *A potential modelling strategy for pressure fluctuations*

Modelling pressure fluctuations in compressible turbulent flows is a challenging task due to the strong coupling of different modes and inherent nonlinearity (Danish, Suman & Srinivasan 2014). However, with the scaling relations for pressure components found in § 3.3, there is a potential modelling strategy for pressure fluctuation intensity p'^+_{rms} by, respectively, modelling pressure components as a function of M. Initially, due to the square

relation $\overline{p'^2} = \overline{p_i^2} + 2\overline{p_i p_c} + \overline{p_c^2}$, the role of the interactions between hydrodynamic and compressible pressure $\overline{p_i p_c}$ is assessed, as shown in figure 11. When compared with the mean square of pressure fluctuations $\overline{p'^2}$, the interactions $\overline{p_i p_c}$ are very weak and can be reasonably disregarded for all cases. This conclusion is also supported by our previous study (Zhang *et al.* 2022) that the interactions between each component are also very weak. As a result, only the two independent components p_i and p_c need to be considered for modelling, and then

$$p'^{+}_{rms}(M) \simeq \sqrt{(p^{+}_{i,rms})^2 + (p^{+}_{c,rms}(M))^2}. \tag{3.8}$$

The current data for $p^{+}_{i,rms}$ and $p^{+}_{c,rms}$ presented in figure 9 are used to construct the model describing the relation between pressure fluctuation intensity and Mach number, denoted as $p'^{+}_{rms}(M)$. Due to the specific and approximately the same Re_τ of the DNS data, the Re effects are not considered currently. To account for the multi-inflexion points present in the distribution of $p^{+}_{i,rms}$, a fifth-order rational polynomial is employed to approximate its uniform behaviour. This can be expressed mathematically as follows:

$$p^{+}_{i,rms} = \frac{\sum_{n=0}^{5} a_n \, (y/\delta)^n}{\sum_{n=0}^{5} b_n \, (y/\delta)^n}, \tag{3.9}$$

where the specific values of the two coefficients a_n and b_n are listed in table 4. The distribution of $p^{+}_{c,rms}$ is dependent on M, and it gradually decays to a plateau value $C(M)$ outside of the boundary layer, which can be summarized by the linear relation $C(M) = 0.12M + 0.08$, as shown in figure 5(*b*). After subtracting the plateau value $C(M)$, the remaining part is modelled as a power function, resulting in

$$p^{+}_{c,rms}(M) = \frac{\phi(M)}{(y/\delta)^{\psi(M)} + \theta(M)} + C(M). \tag{3.10}$$

Based on linear fittings, the assumed relations of these parameters can be determined as

$$\phi(M) = 7.88 \times 10^{-3} M + 3.13 \times 10^{-2}, \tag{3.11a}$$

$$\psi(M) = -1.97 \times 10^{-1} M + 2.10, \tag{3.11b}$$

$$\theta(M) = 7.56 \times 10^{-2} M^{-0.596} + 7.03 \times 10^{-2}. \tag{3.11c}$$

By utilizing this modelling strategy, a reasonable, simple and semiempirical model has been obtained to predict the dependence of pressure fluctuation intensity on the Mach number $p'^{+}_{rms}(M)$. The performance of this model is illustrated in figure 12. The fifth-order rational polynomial accurately replicates the distribution of hydrodynamic pressure. Furthermore, the model effectively captures the increasing features of compressible pressure both near the wall and out of the boundary layer. As a result, the model can successfully predict the distribution trend of pressure fluctuation intensity in a wide range Mach number, as demonstrated in figure 12(*c*). It can be seen that modelling pressure with the help of reasonable means of pressure decomposition is a very feasible way. When mapping the compressible profile of pressure fluctuations to the incompressible counterpart, the contribution of the acoustic mode, which needed to be removed, can also be conveniently given by the model (3.10). To quantitatively assess the performance of the

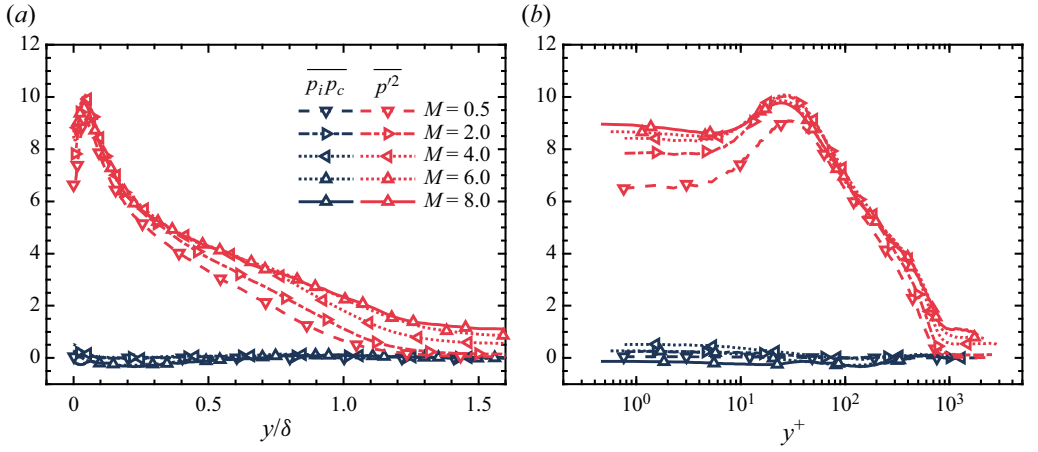

Figure 11. Comparisons of intensities of pressure fluctuations $\overline{p'^2}$ and interactions between pressure components $\overline{p_i p_c}$ in (*a*) the outer scale and (*b*) the inner scale.

n	0	1	2	3	4	5
a_n	1.38×10^{-3}	-2.34×10^{-2}	1.52	-9.08×10^{-2}	−1.50	0.68
b_n	5.70×10^{-4}	-1.07×10^{-2}	0.49	0.98	−1.84	1.00

Table 4. Coefficients of the rational polynomial for modelling the profile of hydrodynamic pressure.

current model, following Griffin *et al.* (2021) the integral relative error is written as

$$\epsilon = 100 \frac{\int_0^{1.5\delta} |P_M - P_D| \, \mathrm{d}y}{\int_0^{1.5\delta} P_D \, \mathrm{d}y}, \tag{3.12}$$

where P_M and P_D denote the profiles obtained from the current model and DNS data, respectively. The integral range is chosen from the wall to slightly beyond the boundary ($y/\delta = 1.5$) to encompass the entire stages of both rapid change and reaching a steady level of pressure fluctuations. The reference data are obtained from Bernardini & Pirozzoli (2011) and Duan *et al.* (2016) with a similar moderate Reynolds number $Re_\tau \approx 500$. Figure 12(*d*) demonstrates that our model performs well, whether based on our own data or the reference DNS data, with a maximum error of approximately $\epsilon \approx 7\,\%$. The relatively larger errors at $M = 4$ and 6 are primarily attributed to the inaccuracies in the linear relationship of $p'^+_{rms,\infty}$ depicted in figure 5(*b*).

4. Summary and discussion

The study investigates the scaling relations between pressure fluctuations and Mach number M in compressible TBLs by examining their generation mechanisms. A comprehensive dataset of DNS with a broad range of $0.5 \leq M \leq 8.0$ and comparable friction Reynolds numbers is analysed. By employing the Van Driest transform and Morkovin scaling, the turbulent statistics of velocity fields for different Mach numbers can be effectively mapped onto their incompressible counterparts. Concerning pressure fluctuation intensity, the profiles exhibit scattering, and the intensities generally increase

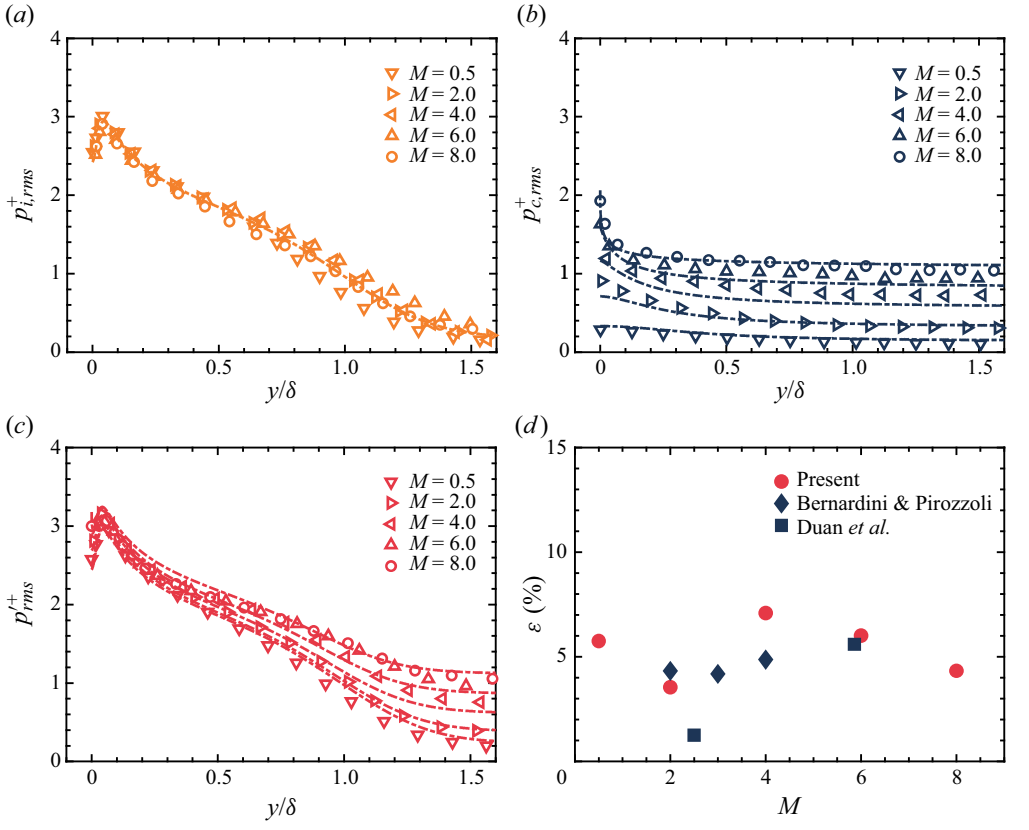

Figure 12. Semiempirical models of fluctuation intensities for (*a*) hydrodynamic pressure $p^+_{i,rms}$; (*b*) compressible pressure $p^+_{c,rms}$ and (*c*) pressure p'^+_{rms}. The symbols denote DNS data, the lines denote the results of the model. (*d*) Integral relative errors with reference data from Bernardini & Pirozzoli (2011) and Duan, Choudhari & Zhang (2016).

with increasing M due to the amplification of genuine compressibility effects and acoustic radiations. As indicators of the vorticity mode and acoustic mode, which contribute to the pressure fluctuations, vorticity fluctuation intensities are minimally affected by increasing M, while dilatation fluctuation intensities monotonically increase with increasing M.

Based on the governing equation of pressure fluctuations, these fluctuations are decomposed into distinct components, each corresponding to the characteristics of different source terms and representing different generation mechanisms. The compressible component denotes the contributions of compressibility effects capturing the physics of acoustic waves, and the sum of the rest components is defined as hydrodynamic pressure relating to the contributions of convective vortex structures. This decomposition achieves a reasonable distinction between the contributions to pressure fluctuations from acoustic and vorticity modes. The convection velocity of hydrodynamic pressure agrees with the typical value of convecting vortices ($u_c \approx 0.6u_\infty$), while for compressible pressure, it increases to the typical value of acoustic waves ($u_c \approx 0.6u_\infty + a_w$). It is observed that the intensities of hydrodynamic pressure exhibit a uniform profile, collapsing with their incompressible counterpart. In contrast, the intensities of compressible pressure are monotonically enhanced with increasing M. These scaling relations agree with the observations on intensities of vorticity and dilatation fluctuations. Hence, the profiles

of pressure fluctuation intensities in compressible TBLs can be mapped onto their incompressible counterparts by removing the contribution from the acoustic mode, as denoted by compressible pressure. In addition, the interactions between the hydrodynamic and compressible pressure are assessed to be negligibly weak compared with original pressure fluctuations. With the identified scaling relations of the hydrodynamic and compressible pressure, a potential modelling strategy for pressure fluctuations that, respectively, models the pressure components is proposed and applied by fitting the DNS data.

It is worth noting that although the present study is conducted by analysing compressible TBLs at the moderate friction Reynolds number $Re_\tau \approx 630$, the explored scaling relations should be qualitatively general in fully developed compressible TBLs since increasing Reynolds numbers do not change the physical natures of the acoustic mode and vorticity mode. Future studies at higher Re_τ are necessary to explore the influence of Reynolds number effects on the characteristics of the two pressure components.

Acknowledgements. The numerical computations were performed at Hefei Advanced Computing Center.

Funding. This work was supported by the National Natural Science Foundation of China under grant nos. 12402258, 12322210, 92252202, 12172351 and 12388101; the Strategic Priority Research Program of Chinese Academy of Sciences, grant no. XDB0620201; and the Fundamental Research Funds for the Central Universities.

Declaration of interests. The authors report no conflict of interest.

Author ORCIDs.
Peng-Jun-Yi Zhang https://orcid.org/0000-0002-0554-9049;
Zhen-Hua Wan https://orcid.org/0000-0003-0035-3116;
Xi-Yun Lu https://orcid.org/0000-0002-0737-6460.

References

ADAMS, N.A. 1998 Direct numerical simulation of turbulent compression ramp flow. *Theor. Comput. Fluid Dyn.* **12** (2), 109–129.

ANANTHARAMU, S. & MAHESH, K. 2020 Analysis of wall-pressure fluctuation sources from direct numerical simulation of turbulent channel flow. *J. Fluid Mech.* **898**, A17.

BERESH, S.J., HENFLING, J.F., SPILLERS, R.W. & PRUETT, B.O.M. 2011 Fluctuating wall pressures measured beneath a supersonic turbulent boundary layer. *Phys. Fluids* **23** (7), 075110.

BERNARDINI, M., MODESTI, D., SALVADORE, F. & PIROZZOLI, S. 2021 STREAmS: a high-fidelity accelerated solver for direct numerical simulation of compressible turbulent flows. *Comput. Phys. Commun.* **263**, 107906.

BERNARDINI, M. & PIROZZOLI, S. 2011 Wall pressure fluctuations beneath supersonic turbulent boundary layers. *Phys. Fluids* **23** (8), 085102.

BULL, M.K. 1996 Wall-pressure fluctuations beneath turbulent boundary layers: some reflections on forty years of research. *J. Sound Vib.* **190** (3), 299–315.

CECI, A., PALUMBO, A., LARSSON, J. & PIROZZOLI, S. 2022 Numerical tripping of high-speed turbulent boundary layers. *Theor. Comput. Fluid Dyn.* **36** (6), 865–886.

CHANG, III, P.A., PIOMELLI, U. & BLAKE, W.K. 1999 Relationship between wall pressure and velocity-field sources. *Phys. Fluids* **11** (11), 3434–3448.

CHASE, D.M. 1980 Modeling the wavevector-frequency spectrum of turbulent boundary layer wall pressure. *J. Sound Vib.* **70** (1), 29–67.

CHASE, D.M. 1987 The character of the turbulent wall pressure spectrum at subconvective wavenumbers and a suggested comprehensive model. *J. Sound Vib.* **112** (1), 125–147.

CORCOS, G.M. 1963 Resolution of pressure in turbulence. *J. Acoust. Soc. Am.* **35** (2), 192–199.

DANISH, M., SUMAN, S. & SRINIVASAN, B. 2014 A direct numerical simulation-based investigation and modeling of pressure Hessian effects on compressible velocity gradient dynamics. *Phys. Fluids* **26** (12), 126103.

DUAN, L., BEEKMAN, I. & MARTÍN, M.P. 2011 Direct numerical simulation of hypersonic turbulent boundary layers. Part 3. Effect of Mach number. *J. Fluid Mech.* **672**, 245–267.

DUAN, L., CHOUDHARI, M.M. & WU, M. 2014 Numerical study of acoustic radiation due to a supersonic turbulent boundary layer. *J. Fluid Mech.* **746**, 165–192.

DUAN, L., CHOUDHARI, M.M. & ZHANG, C. 2016 Pressure fluctuations induced by a hypersonic turbulent boundary layer. *J. Fluid Mech.* **804**, 578–607.

FOYSI, H., SARKAR, S. & FRIEDRICH, R. 2004 Compressibility effects and turbulence scalings in supersonic channel flow. *J. Fluid Mech.* **509**, 207–216.

GEROLYMOS, G.A., SÉNÉCHAL, D. & VALLET, I. 2007 Wall-effects on pressure fluctuations in quasi-incompressible and compressible turbulent plane channel flow. In *37th AIAA Fluid Dynamics Conference and Exhibit*, p. 3863. AIAA paper.

GEROLYMOS, G.A., SÉNÉCHAL, D. & VALLET, I. 2013 Wall effects on pressure fluctuations in turbulent channel flow. *J. Fluid Mech.* **720**, 15–65.

GEROLYMOS, G.A. & VALLET, I. 2023 Scaling of pressure fluctuations in compressible turbulent plane channel flow. *J. Fluid Mech.* **958**, A19.

GLOERFELT, X. & BERLAND, J. 2013 Turbulent boundary-layer noise: direct radiation at Mach number 0.5. *J. Fluid Mech.* **723**, 318–351.

GRASSO, G., JAISWAL, P., WU, H., MOREAU, S. & ROGER, M. 2019 Analytical models of the wall-pressure spectrum under a turbulent boundary layer with adverse pressure gradient. *J. Fluid Mech.* **877**, 1007–1062.

GRIFFIN, K.P., FU, L. & MOIN, P. 2021 Velocity transformation for compressible wall-bounded turbulent flows with and without heat transfer. *Proc. Natl Acad. Sci.* **118** (34), e2111144118.

GRIFFIN, K.P., FU, L. & MOIN, P. 2023 Near-wall model for compressible turbulent boundary layers based on an inverse velocity transformation. *J. Fluid Mech.* **970**, A36.

HOWE, M.S. 1998 *Acoustics of Fluid–Structure Interactions*. Cambridge University Press.

HU, N., REICHE, N. & EWERT, R. 2017 Simulation of turbulent boundary layer wall pressure fluctuations via Poisson equation and synthetic turbulence. *J. Fluid Mech.* **826**, 421–454.

HUANG, J., DUAN, L. & CHOUDHARI, M.M. 2022 Direct numerical simulation of hypersonic turbulent boundary layers: effect of spatial evolution and Reynolds number. *J. Fluid Mech.* **937**, A3.

JIANG, G.-S. & SHU, C.-W. 1996 Efficient implementation of weighted ENO schemes. *J. Comput. Phys.* **126** (1), 202–228.

JIMÉNEZ, J., HOYAS, S., SIMENS, M. & MIZUNO, Y. 2010 Turbulent boundary layers and channels at moderate Reynolds numbers. *J. Fluid Mech.* **657**, 335–360.

KISTLER, A.L. & CHEN, W.S. 1963 The fluctuating pressure field in a supersonic turbulent boundary layer. *J. Fluid Mech.* **16** (1), 41–64.

LAGANELLI, A.L., MARTELLUCCI, A. & SHAW, L.L. 1983 Wall pressure fluctuations in attached boundary-layer flow. *AIAA J.* **21** (4), 495–502.

LELE, S.K. 1994 Compressibility effects on turbulence. *Annu. Rev. Fluid Mech.* **26** (1), 211–254.

LILLEY, G.M. 1963 Wall pressure fluctuations under turbulent boundary layers at subsonic and supersonic speeds. *Tech. Rep.* 454. AGARD.

MORKOVIN, M.V. 1962 Effects of compressibility on turbulent flows. *Méc. Turbul.* **367** (380), 26.

PHILLIPS, O.M. 1960 On the generation of sound by supersonic turbulent shear layers. *J. Fluid Mech.* **9** (1), 1–28.

PIROZZOLI, S. 2010 Generalized conservative approximations of split convective derivative operators. *J. Comput. Phys.* **229** (19), 7180–7190.

PIROZZOLI, S., BERNARDINI, M. & GRASSO, F. 2010 Direct numerical simulation of transonic shock/boundary layer interaction under conditions of incipient separation. *J. Fluid Mech.* **657**, 361–393.

POINSOT, T.J. & LELE, S.K. 1992 Boundary conditions for direct simulations of compressible viscous flows. *J. Comput. Phys.* **101** (1), 104–129.

POPE, S.B. 2000 *Turbulent Flows*. Cambridge University Press.

RITOS, K., DRIKAKIS, D. & KOKKINAKIS, I.W. 2019*a* Acoustic loading beneath hypersonic transitional and turbulent boundary layers. *J. Sound Vib.* **441**, 50–62.

RITOS, K., DRIKAKIS, D. & KOKKINAKIS, I.W. 2019*b* Wall-pressure spectra models for supersonic and hypersonic turbulent boundary layers. *J. Sound Vib.* **443**, 90–108.

SARKAR, S. 1992 The pressure–dilatation correlation in compressible flows. *Phys. Fluids* A **4** (12), 2674–2682.

SMITS, A.J. 1991 Turbulent boundary-layer structure in supersonic flow. *Proc. R. Soc. Lond.* A **336** (1641), 81–93.

SPALART, P.R., MOSER, R.D. & ROGERS, M.M. 1991 Spectral methods for the Navier–Stokes equations with one infinite and two periodic directions. *J. Comput. Phys.* **96** (2), 297–324.

TANG, J., ZHAO, Z., WAN, Z.-H. & LIU, N.-S. 2020 On the near-wall structures and statistics of fluctuating pressure in compressible turbulent channel flows. *Phys. Fluids* **32** (11), 115121.

TRETTEL, A. & LARSSON, J. 2016 Mean velocity scaling for compressible wall turbulence with heat transfer. *Phys. Fluids* **28** (2), 026102.

VAN DRIEST, E.R. 1951 Turbulent boundary layer in compressible fluids. *J. Aeronaut. Sci.* **18** (3), 145–160.

VOLPIANI, P., IYER, P., PIROZZOLI, S. & LARSSON, J. 2020 Data-driven compressibility transformation for turbulent wall layers. *Phys. Rev. Fluids* **5**, 052602.

WILLMARTH, W.W. 1975 Pressure fluctuations beneath turbulent boundary layers. *Annu. Rev. Fluid Mech.* **7** (1), 13–36.

XU, D., WANG, J. & CHEN, S. 2022 Skin-friction and heat-transfer decompositions in hypersonic transitional and turbulent boundary layers. *J. Fluid Mech.* **941**, A4.

YANG, B. & YANG, Z. 2022 On the wavenumber–frequency spectrum of the wall pressure fluctuations in turbulent channel flow. *J. Fluid Mech.* **937**, A39.

YU, M., XU, C.-X. & PIROZZOLI, S. 2020 Compressibility effects on pressure fluctuation in compressible turbulent channel flows. *Phys. Rev. Fluids* **5** (11), 113401.

ZHANG, C., DUAN, L. & CHOUDHARI, M.M. 2017 Effect of wall cooling on boundary-layer-induced pressure fluctuations at Mach 6. *J. Fluid Mech.* **822**, 5–30.

ZHANG, P.-J.-Y., WAN, Z.-H., DONG, S.-W., LIU, N.-S., SUN, D.-J. & LU, X.-Y. 2023 Conditional analysis on extreme wall shear stress and heat flux events in compressible turbulent boundary layers. *J. Fluid Mech.* **974**, A38.

ZHANG, P.-J.-Y., WAN, Z.-H., LIU, N.-S., SUN, D.-J. & LU, X.-Y. 2022 Wall-cooling effects on pressure fluctuations in compressible turbulent boundary layers from subsonic to hypersonic regimes. *J. Fluid Mech.* **946**, A14.

ZHAO, Z., LIU, N.-S. & LU, X.-Y. 2020 Kinetic energy and enstrophy transfer in compressible Rayleigh–Taylor turbulence. *J. Fluid Mech.* **904**, A37.